
Article:
Li, P., Jiang, W., Susmel, L. orcid.org/0000-0001-7753-9176 et al. (1 more author) (2023) Porosity-related high-cycle fatigue strength of nickel-base single crystals: fatigue experiments and Electron Back-scattered Diffraction analysis. International Journal of Fatigue, 168. 107374. ISSN 0142-1123

https://doi.org/10.1016/j.ijfatigue.2022.107374

Porosity-related high-cycle fatigue strength of nickel-base single crystals: fatigue experiments and Electron Back-scattered Diffraction analysis

Piao Li[a,b *], Wen Jiang[c,d], Luca Susmel[a], Qi-nan Han[e,f]

[a] *Department of Civil and Structural Engineering, The University of Sheffield, Sheffield S1 3JD, UK*

[b] *College of Aerospace Engineering, Nanjing University of Aeronautics and Astronautics, Nanjing 210016, China*

[c] *Nanjing Engineering Institute of Aircraft Systems, AVIC, Nanjing 211106, China*

[d] *Aviation Key Laboratory of Science and Technology on Aero Electromechanical System Integration, Nanjing 211106, China*

[e] *College of Energy and Power Engineering, Nanjing University of Aeronautics and Astronautics, Nanjing 210016, China*

[f] *Aero-Engine Thermal Environment and Structure Key Laboratory of Ministry of Industry and Information Technology, Nanjing 210016, China*

* Corresponding author : lipiao@nuaa.edu.cn

Abstract: The fatigue limit of nickel-base single crystal (NBSX) is experimentally studied at an elevated temperature of 980°C. The crack initiation position is revealed as the casting pores in the single crystal under scanning electron microscope (SEM), and distinct “fish-eye” region is observed on the long cycle fatigue fracture surface. The failure mechanism is explored around the “fish-eye” by adopting the focused ion beam (FIB) and electron backscatter diffraction (EBSD) technique. The crystalline motion and the fatigue crack initiation mechanism around the initiation pore are revealed by conducting microscopic analyses.

Key words: Nickel-base single crystal; Fatigue limit; Failure mechanism; Crack initiation

1. Introduction

Nickel-base single crystals (NBSX) have long been used for the fabrication of hot-end components such as the turbine blades due to their excellent fatigue and creep resistance at elevated-temperature [1]. Owing to the elimination of grain boundary where cracks are prone to initiate, the

high-temperature anti-fatigue capacity of NBSXs has been enhanced. However, this specific single crystal structure requires a complicated casting process. Nowadays the directional solidification technique is commonly used for the casting of NBSXs, and currently it is inevitable to avoid the introduction of casting pores in the solidification process. As an unavoidable internal defect, pores become the stress concentration locations under external loading, and replace the grain boundary as the place where fatigue cracks are prone to initiate [2, 3].

The working environment of NBSX components is often under high temperature and high pressure, and fatigue failure is one of the most common engineering problems [4, 5]. At present, the research on the fatigue problems of NBSX involves orientation-related anisotropic fatigue properties [6-8], the influence and mechanism of different working environment or load conditions on its fatigue failure mode [9-12], creep-coupled or thermomechanical fatigue problems [5, 13-15], the influence of casting process parameters and alloy composition on fatigue properties [16], the development of fatigue life prediction models[17-20], etc. The effect of non-zero mean stress on the fatigue life of NBSX has also attracted attention. The effect of non-zero mean stress on the fatigue life of NBSX has also attracted attention. Wan et al. studied the low-cycle fatigue (LCF) behavior of smooth and notched specimens of a NBSX and proposed a crystallographic LCF life model that considers mean stress effect [21]. Li et al. developed a mean stress modified strain range partitioning method to predict the fatigue-creep life of NBSX SRR99 and put forward the idea that the mean stress effect plays a role in the influences of strain dwells on the life of SRR99 [22]. Brien et al. experimentally studied the deformation microstructures of a NBSX in LCF, and the microstructures of the crystal under both zero and non-zero mean stress conditions are studied in detail [23]. The fatigue endurance limit is a critical parameter regarding the engineering anti-fatigue design, and

currently few studies can be found on this aspect. Ryan and Patrick [24] studied the fatigue behavior of a NBSX superalloy in the gigacycle regime of 10^6 to 10^9 cycles at an immediate temperature of 593°C. By comparing their tested endurance limit under a high frequency of 20kHz with similar data generated near 60Hz, they come to the conclusion that there is little or no frequency effect on the fatigue limit or failure mechanisms of the tested NBSX. Existing studies [12, 25, 26] have shown that temperature has a significant effect on the fatigue failure mode of NBSXs, even though the coupling effect of temperature and loading frequency is not clear yet. Therefore, the failure morphology and mechanism obtained by Ryan and Patrick at medium temperature cannot directly be applied to the near-fatigue-limit study of NBSXs at high temperature. Belyaev et al. [27, 28] experimentally studied the high cycle fatigue limit of NBSXs, and they found that the anisotropy of the high cycle fatigue limit of tested NBSXs is insignificant. Jiang et al. [29] obtained some specially-casted NBSXs with different pore sizes by controlling the casting process, and used them to study the conditional fatigue limit. Combining the life prediction model with Murakami's model, a fatigue limit evaluation approach was proposed. The above research carries out the defect-tolerance analysis by combing with the Kitagawa-Takahashi diagram, which can be very practical for engineering purpose. Based on previous studies, this research concentrates on the high-temperature fatigue limit of NBSXs obtained under normal casting process and focuses on the damage mechanism of high cycle fatigue near the fatigue limit by using different research methods.

The study on conditional fatigue limit is often included in the study of ultra-high cycle fatigue. At present, some research has been conducted on the ultra-high cycle fatigue damage mechanism of NBSXs. Cervellon [30] et al. investigated the crack initiation mechanism in the ultra-high cycle fatigue regime of NBSXs at high temperature and under fully reversed loading conditions. They

identified for the first time a discernible area called rough zone around the crack initiation site, and conducted detailed research on the relevant failure mechanism. Crack initiation generally occupies a large endurance part in the entire fatigue failure process, and it is significant to further investigate the very initial failure mechanism by analyzing the observed discernible area around the crack initiation site [31]. In fact, similar observations have long been noticed and studied in the very high cycle fatigue of other materials undergoing different names among which the best known ones are fine granular area (FGA) and fish-eye region [32]. Grad et al. [33] identified the FGA on the fracture surfaces of high-strength steels after very high cycle fatigue loading, and proposed a mechanism for the formation of this area by means of multiple microscopic investigations. Heinz and Eifler [34] conducted high frequency fatigue tests to study the very high cycle fatigue behavior of a titanium alloy, and the fracture surfaces under light and scanning electron microscopy are characterized by fish eye structure. Though multiple formation mechanism of the FGA has been proposed [35-39], at present a widely accepted mechanism does not exist. Besides, considering the difference in material composition and crystallographic structure, as well as the diversity of external factors that can affect the FGA formation and morphology [40-42], it is of essential significance to conduct specific research on the formation of this distinct region in NBSXs, and at present, there is still a lack of research from this aspect.

In recent years, the misorientation analysis based on EBSD technology has gradually become an effective failure analysis method [43-45]. The theoretical basis or working principle of EBSD is to conduct orientation based post-processing analysis by obtaining the orientation information of every micro-area on the sample. In the field of applied mechanics, this technology has been applied to failure analysis of tension [46-50], creep [51, 52] and fatigue [53-55]. Compared with the

traditional fracture analysis methods, EBSD can effectively obtain the internal deformation features of the crystal, and avoid the influence of environmental factors such as the effect of oxidation on the fracture surface. Especially for single crystal materials, the undeformed material has an orderly crystal structure. EBSD has the advantage of effectively obtaining the crystal orientation changes caused by internal deformation such as lattice torsion after loading, providing a new perspective for the analysis of fatigue damage mechanism. In order to characterize the above-mentioned deformation information which is represented by orientation changes, orientation-related parameters such as Kernel Averaged Misorientation (KAM) and Grain Reference Orientation Deviation (GROD), which will be introduced in detail in Section 3, can be adopted and the achievability of their visualization through mapping methods can give a direct quantifiable presentation of the deformation degree in material failure process. Above all, the adoption of EBSD in the study of single crystal fatigue failure is rational and effective. At present, there are few studies on the application of EBSD to the fatigue damage analysis of NBSXs. Ruttert et al. [56] adopted the EBSD to investigate the influence of eutectics and porosity on the high-temperature LCF life of a NBSX, and come to the conclusion that both pores and eutectics have a negative impact on the LCF performance. Han et al. [57] used the EBSD to study the effect of crystal orientation on fretting fatigue induced crack initiation and dislocation distribution, and their EBSD analysis results could show obvious misorientation and orientation deviation in the fretting contact area. Moverare et al. [14] studied the deformation and damage mechanisms arising during thermal–mechanical fatigue of a NBSX, and the EBSD map was adopted and proven a useful tool to show the recrystallization and misorientation. In fact, EBSD technique can do much more than being used as an orientation expression method. The deformation information can be extracted and processed from the original

orientation data, and then used for the damage characterization. Up till now, there is still a lack of research on the deformation characterization and fatigue failure mechanism of NBSXs by applying the EBSD techniques.

In this paper, the up-down test of a NBSX superalloy is carried out at an elevated temperature to obtain the fatigue limit, and the deformation mechanism is investigated by conducting in-depth failure analysis around the crack initiation site where “fish-eye” is observed. The EBSD technique is adopted to analyze the dislocation motion and lattice distortion during the damage process.

2. Up-Down Experiment

2.1 Test method

Up-down experiment is a testing method used to obtain the conditional fatigue limit of materials. The real fatigue limit does not exist [58], and the so-called conditional fatigue limit refers to the fatigue strength corresponding to a certain cycle of fatigue. Generally the fatigue limit corresponding to 10^7 fatigue cycles is commonly used in engineering, and thus in this paper, the so-called fatigue limit refers to the loading magnitude that causes a fatigue failure at 10^7 cycles.

In the current up-down test, the failure cycles 10^7 is set as the termination condition of a single test: if a test piece fails before 10^7 cycles, the test is terminated, and this test point is defined as a failure point (×). Otherwise if a test piece does not fail before 10^7 cycles, the test is terminated at 10^7 cycles, and this test point is defined as a pass point (○). If the previous test piece makes a pass point, the subsequent test piece is loaded under a lower stress level. If the previous test piece makes a failure point, the subsequent test piece is loaded under a higher stress level. The determination of the stress increment/decrement will be introduced in next section. The test rule stands until all the

tests are completed. The first effective data point is the point where the opposite test results (failure and pass) appear for the first time. After all the tests, all the opposite data points are matched and the mean value and standard deviation of the fatigue limit are calculated according to the following equation

$$\begin{aligned} S_{\mathrm{m}} &= \frac{1}{n_{\mathrm{S}}}\sum_{i=1}^{n_{\mathrm{S}}} S_i \\ S_i &= \frac{S_{\mathrm{F}} + S_{\mathrm{p}}}{2} \\ S_{\mathrm{s}} &= \sqrt{\frac{1}{n_{\mathrm{S}} - 1}\sum_{i=1}^{n_{\mathrm{S}}} (S_i - S_{\mathrm{m}})^2} \end{aligned} \tag{1}$$

where S_i denotes a couple of opposite test points, S_{F} and S_{P} separately denotes the stress magnitude of the failure point and the pass point in a couple. n_s is the number of couples. S_{m} and S_{S} respectively represents the mean value and standard deviation of the fatigue limit.

2.2 Material and test piece

The test material is second generation NBSX superalloy DD5 developed in China. Since 3% Re has been added on the basis of the first generation, its ability to withstand high temperature loading is further improved. The nominal composition of the alloy is shown in Table 1. The tensile strength in [001] direction at 980 ° C and the engineering elastic constants in [001] direction at 1000 ° C are shown in Table 2.

Table 1

Nominal composition of DD5 (in wt.%).

Cr	Co	Mo	W	Ta	Re	Hf	Al	C	Ni
7	8	2	5	7	3	0.2	6.2	0.05	Balance

Table 2

Mechanical properties of DD5 (in [001] direction)

Elastic modulus *E*/GPa	Poisson's ratio μ	Shear modulus *G*/GPa	Yield strength $\sigma_{0.2}$ /MPa	Ultimate strength σ_b /MPa
95.34	0.416	89.7	792	850

The test bars are produced by using the spiral grain selection in a high gradient vacuum induction furnace. The heat treatment process of as-cast test bars is 1310°C/2h + 1313°C/2h (air cooling) + 1130°C/4h + 870°C/16h (air cooling). The original test bars have a main orientation of [001] with different misorientation degrees. Due to the inevitability of misorientation in the current casting process [59, 60], and the well-accepted theory that fatigue performance can be weakened by increasing misorientation degree [6, 61, 62], the axial crystal orientation of the test bars is selected to be less than 5° after the orientation measurement under EBSD.

The geometry of the test specimen is shown in Fig.1. The hourglass shaped test piece has a total length of 70mm, and the clamping section at the two ends is 14mm in length and 14mm in diameter. The diameter of the gauge section gradually decreases from both ends to the middle, and the diameter at the middle minimum section is 5mm.

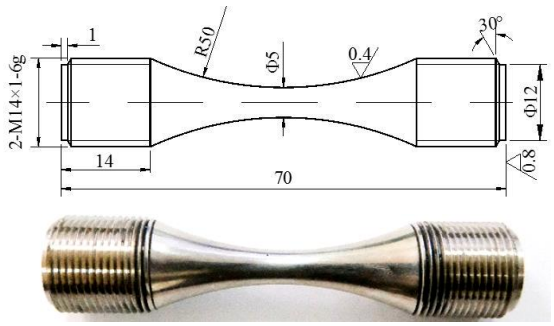

Fig.1. Configuration of test piece (Unit:mm)

2.3 Test process

The fatigue tests were carried out on the GBQ50-B high frequency fatigue testing machine, as shown in Figure 2. The maximum loading capacity of the testing machine is ±50KN . The loading frequency was set equal to 110Hz and the test temperature to 980 °C. Before the test, the specimens were clamped in the testing machine through the fixtures, and a thermocouple was attached at the center of the specimen for temperature measurement. The test pieces were placed in a high-temperature furnace to be preheated to 980 °C before the test. The test pieces were not loaded until the temperature was stable with a fluctuation less than ±3 °C. The loading waveform was a sine wave, and the stress ratio was set equal to 0.1. The test conditions are summarized in Table 3.

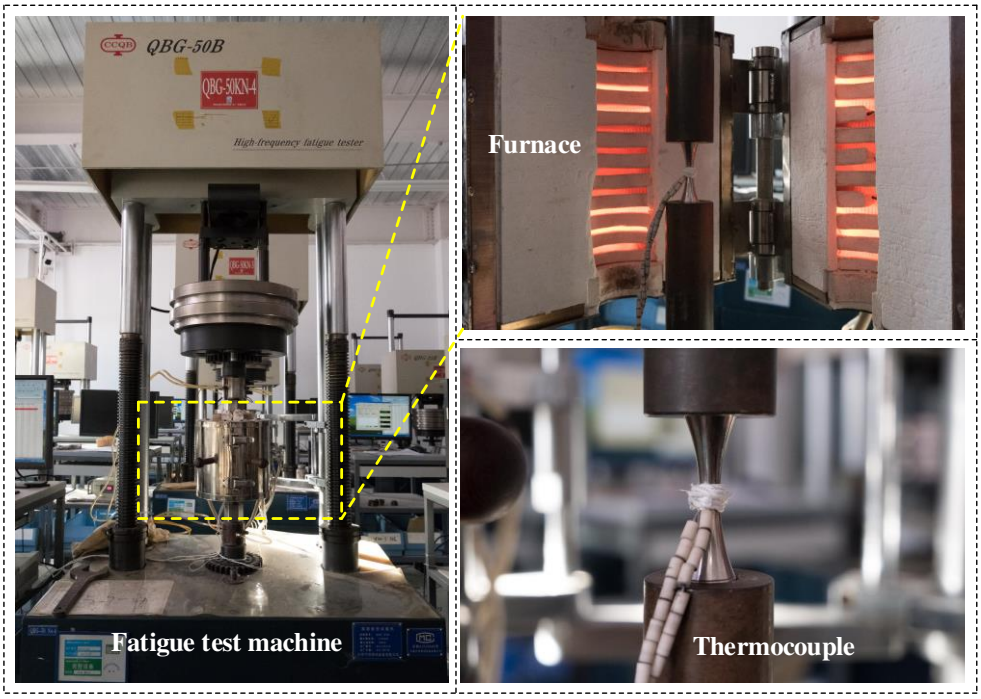

Fig.2. Fatigue test implementation

Table 3

Up-down test conditions.

Test temperature	Loading frequency	Load wave	Stress ratio

980 °C	110Hz	Sine	0.1

In order to use the up-down test method, it is necessary to determine the stress increment/decrement to define pass and failure points. This value is kept constant throughout the whole test process, and it is referred to as stress variation hereinafter. Generally, the stress variation should be determined as less than 5% of the fatigue limit [63]. According to the mechanical properties listed in Table 2, the fatigue limit of the NBSX DD5 was estimated to be equal to 50% of the tensile strength, namely 425 MPa. Accordingly, the stress variation had to be less than 21.25 MPa. Therefore, in order to obtain a more precise value of the fatigue limit from the test, the stress variation was taken equal to 10MPa.

2.4 Test results and fracture analysis

The up-down test results are shown in Fig.3. The first effective point starts from the stress level of 440MPa. The calculated fatigue limit according to Eq. (1) is 432.5MPa. There are in total 4 fractured specimens and three failed at 440MPa and one failed at 430MPa.

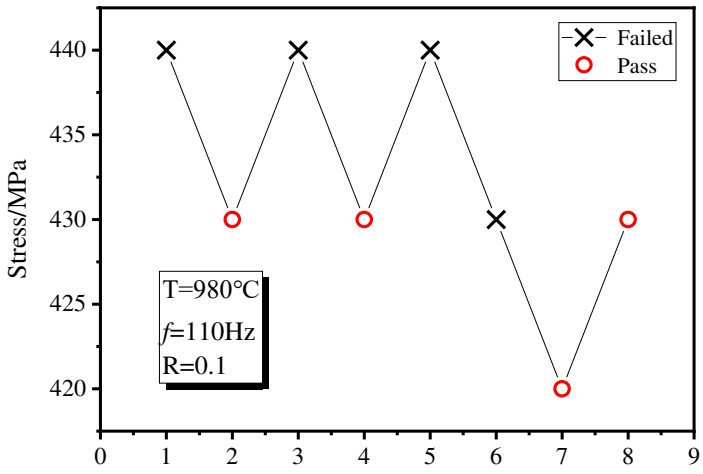

Fig.3. Up-down test result

The fracture surfaces of the four specimens are shown in Fig.4. It can be seen clearly from the

fracture surface that the crack initiates from the casting pore, and there exists a visually distinguishable round-like area around the pore. Since it is very similar to the fish-eye region on the fracture surface of the VHCF specimen, hereinafter this region is referred to as fish-eye region.

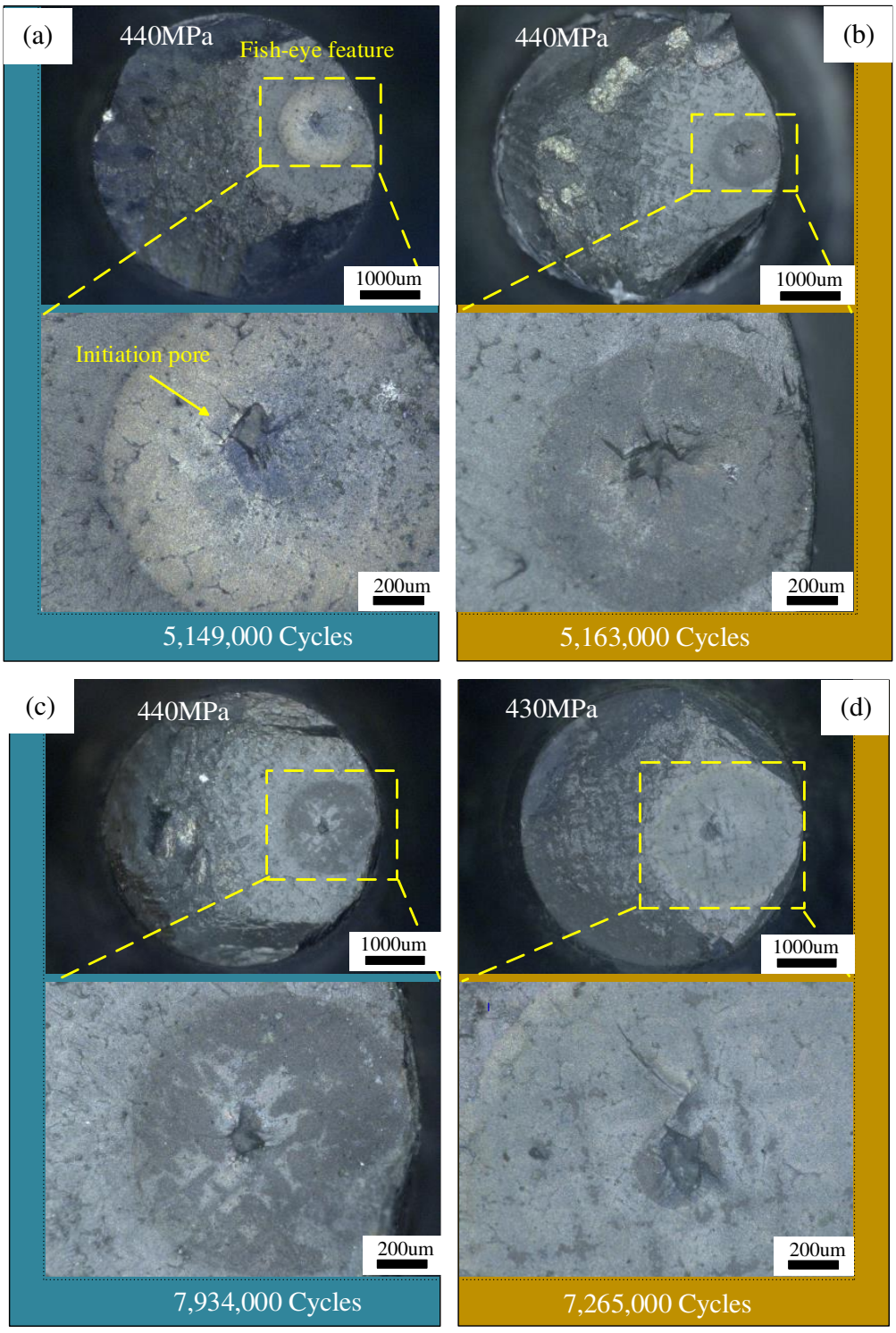

Fig.4. Fracture surface

Our previous study has shown that pore size has a significant effect on the fatigue life of NBSX [29]. Murakami's diameter [64] and Feret's diameter [65] are both adopted here to quantify the pore size. Murakami's diameter is the root-mean-square of the projected area of the pore, whereas Feret's diameter is the diameter of the smallest circle that contains the pore, as shown in Fig.5.

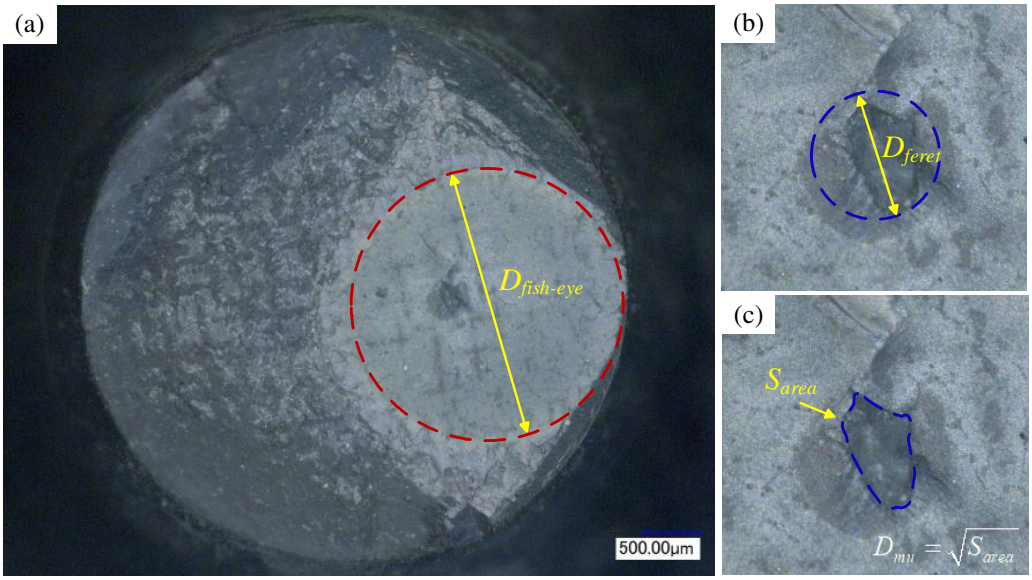

Fig. 5. Crack initiation region characterization: (a) Fish-eye size (b) Feret diameter (3) Murakami diameter

The measured pore size as well as the fish-eye region size are listed in Table 4. It can be seen that the cycles are correlated with the pore size and stress level. When the pore size is bigger, and the stress is higher, the cycles are lower. The fish-eye size shows a stronger dependence on the stress.

Table 4

Test and measurement data. (Note: Test No. 2,4,7,8 are unfractured specimens)

Test No.	1	2	3	4	5	6	7	8
Stress/MPa	440	430	440	430	440	430	420	430
Cycles	5,149,000	---	5,163,000	---	7,934,000	7,265,000	---	---
S_{area}/ um^2	24357	---	26572	---	14786	33013	---	---

$D_{Mu}(\sqrt{S_{area}})$/ um	156	---	163	---	122	182	---	---
D_{feret} / um	241	---	235	---	195	302	---	---
$D_{fish\text{-}eye}$ / um	1518	---	1143	---	1639	2558	---	---

3. EBSD implementation

3.1 Misorientation characterization parameter (KAM and GROD)

The EBSD technique provides a practical method to detect the orientation alteration in the single crystal. The original data obtained from the EBSD are in the form of Euler angle （ϕ_1, ϕ, ϕ_2）, which can be further transformed into the form of orientation matrix $\boldsymbol{g}$,

$$g=\begin{bmatrix}\cos\phi_2 & \sin\phi_2 & 0\\ -\sin\phi_2 & \cos\phi_2 & 0\\ 0 & 0 & 1\end{bmatrix}\begin{bmatrix}1 & 0 & 0\\ 0 & \cos\phi & \sin\phi\\ 0 & -\sin\phi & \cos\phi\end{bmatrix}\begin{bmatrix}\cos\phi_1 & \sin\phi_1 & 0\\ -\sin\phi_1 & \cos\phi_1 & 0\\ 0 & 0 & 1\end{bmatrix} \tag{2}$$

Therefore, the orientation deviation between any two points A and B can be obtained through the following equation,

$$\theta_{\mathrm{A}}^{\mathrm{B}}=\arccos\left[\frac{trace(g_{\mathrm{B}}\cdot g_{\mathrm{A}}^{-1})-1}{2}\right] \tag{3}$$

For single crystal materials, few orientation deviation can be found in the undeformed state. However, after the material undergoes a damage process which can cause severe local deformation, the lattice can no longer maintain its original regular form and leads to varied orientation distribution in the single crystal. In order to characterize the degree of transgranular orientation variation, two parameters were introduced: the Kernel Averaged Misorientation (KAM) and the Grain Reference Orientation Deviation (GROD).

KAM is defined as the average misorientation degree between the kernel point with respect to its surrounding points. Generally the surrounding points can be the four (in some cases six or eight) neareast points around the kernel point. According to its definition, the KAM is a parameter used to characterize the local orientation gradient, and it is a reflection of the local deformation degree.

$$\mathrm{KAM}(i,j) \xrightarrow{def} \frac{1}{4}\left(\theta_{(i,j)}^{(i-1,j)} + \theta_{(i,j)}^{(i+1,j)} + \theta_{(i,j)}^{(i,j-1)} + \theta_{(i,j)}^{(i,j+1)}\right) \tag{4}$$

GROD is defined as the orientation deviation between a target point and a reference point. Generally the reference point is taken as the point representing the average orientation state of the crystalline grain [66] or the point with the lowest KAM value. It can be seen from the definition that GROD is a parameter used to characterize the intracrystalline inhomogeneity degree of orientation.

$$\mathrm{GROD}(m,n) \xrightarrow{def} \theta_r^{(m,n)} \tag{5}$$

The schematic of KAM and GROD is shown in Fig.6.

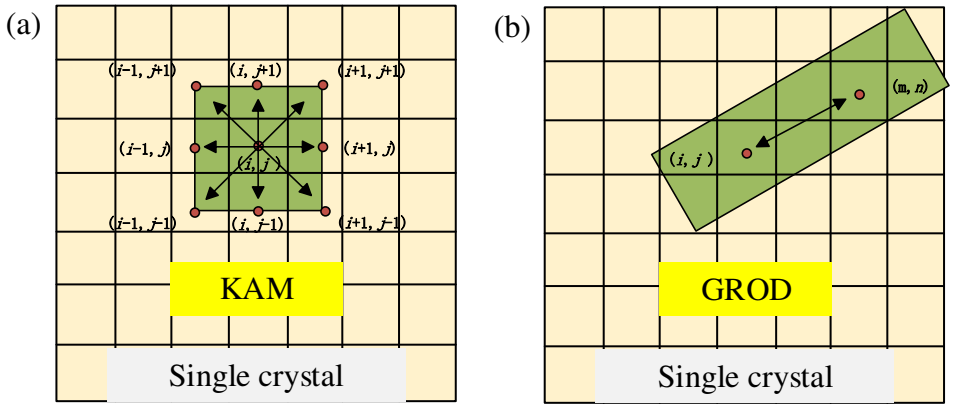

Fig.6. The schematic of (a) KAM and (b) GROD

3.2 Dislocation characterization parameter (GND)

Geometrically Necessary Dislocation (GND) was first introduced by Nye [67], and it refers to the dislocations appeared in strain gradient fields due to geometrical constraints of the crystal lattice in crystals. The GNDs are stored in the crystal microstructure to accommodate the geometrically

deformation gradients, so as to allow compatible deformation of the crystal [68].

Due to the close correlation with lattice curvature, the density of GNDs can be calculated through EBSD. The relation between the local dislocation density tensor $\boldsymbol{\alpha}$ and the curvature tensor $\boldsymbol{\kappa}$ is as follows:

$$\begin{aligned}
\alpha_{12} &= \kappa_{21} \\
\alpha_{13} &= \kappa_{31} \\
\alpha_{21} &= \kappa_{12} \\
\alpha_{23} &= \kappa_{32} \\
\alpha_{33} &= -\kappa_{11} - \kappa_{22} \\
\alpha_{11} - \alpha_{22} &= \kappa_{11} - \kappa_{22}
\end{aligned} \tag{6}$$

The curvature tensor $\boldsymbol{\kappa}$ can be obtained through EBSD. The relation between the local dislocation density tensor $\boldsymbol{\alpha}$ and different dislocation types are [67]:

$$\alpha_{ij} = \sum_{t=1}^{N} b_i^{(t)} l_j^{(t)} \rho^{(t)} \left(i, j = 1,2,3\right) \tag{7}$$

where $\rho^{(t)}$ is the tth type dislocation density, $\mathbf{b}^{(t)}$ and $\mathbf{l}^{(t)}$ are separately the Burgers and line vectors of tth type dislocation.

Thus the curvature tensor $\boldsymbol{\kappa}$ can be expressed as follows:

$$\kappa_{ij} = \sum_{t=1}^{N} \left(b_j^{(t)} l_j^{(t)} - \frac{1}{2} \delta_{ij} b_m^{(t)} l_m^{(t)} \right) \rho^{(t)} \tag{8}$$

where δ_{ij} is the Kronecker delta symbol.

The total GND density is the sum of different dislocation density types:

$$\rho_{\mathrm{GND}} = \sum_{i=1}^{N} \rho^{(t)} \tag{9}$$

3.3 Sample preparation and observation process

In order further to investigate the crack initiation mechanism around the pore, one fractured specimen with typical fish-eye feature was post-processed as an EBSD sample after fatigue testing. Firstly, a small section containing the fractured surface was cut off using wire-electrode cutting,

then this small section was further cut through the center of the pore with very careful attention not to destroy the fracture morphology, as shown in Fig.7(a). It should be noted that the cutting direction was chosen to be along the direction of the dendrite arm, since it is important to locate the lattice coordinate by taking the dendrite arm as a reference, as shown in Fig.4(b). Three observation regions were determined. The first and the second observation sites were located in the optically distinguishable fish-eye region and were at the same cutting edge as the initiation pore. The first observation site was near the edge of the specimen, and the second was in between the first site and the pore. The third observation site was located at the longitudinal section of the specimen, as shown in Fig.7(b).

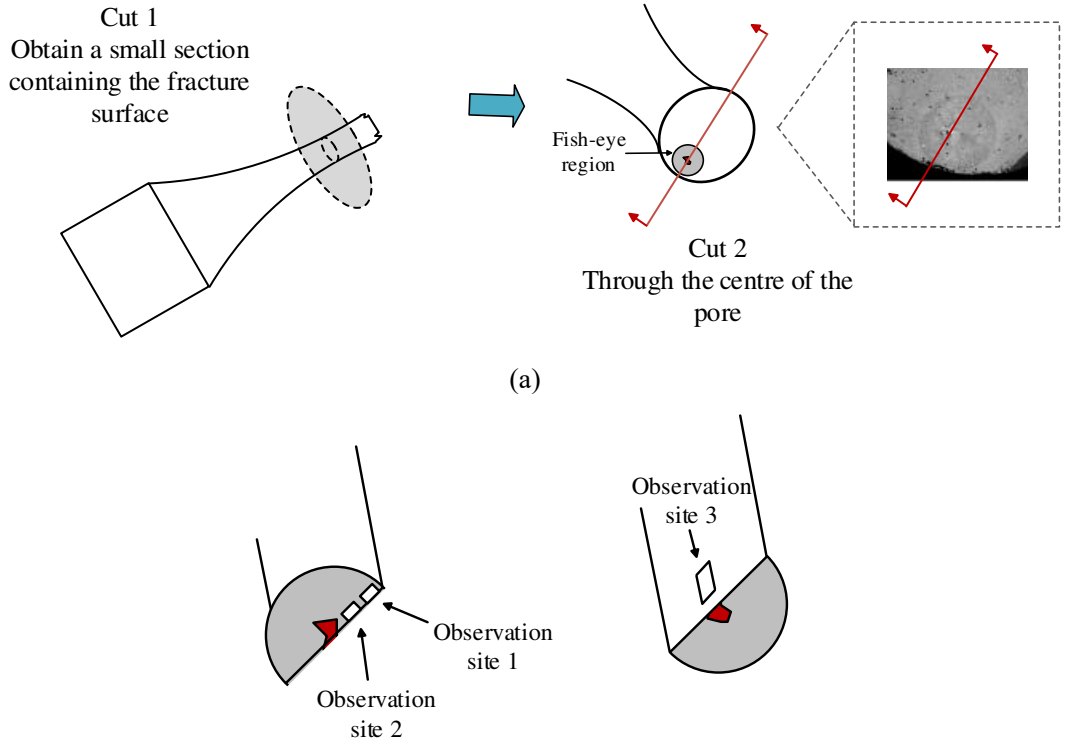

Fig.7. The processing of EBSD observation surface: (a) cutting of the specimen (b) EBSD observation sites

Since the fracture surface can easily be destroyed by using traditional metal polishing methods,

the first two observation sites near the pore were polished by adopting the focused ion beam (FIB) processing through the Strata FIB 201 equipment produced by the America FEI company, as shown in Fig.8. The scan area of the first site was a rectangle with a length of 11.2um and a width of 5um, the scan area of the second site was a rectangle with a length of 11.4um and a width of 5um.

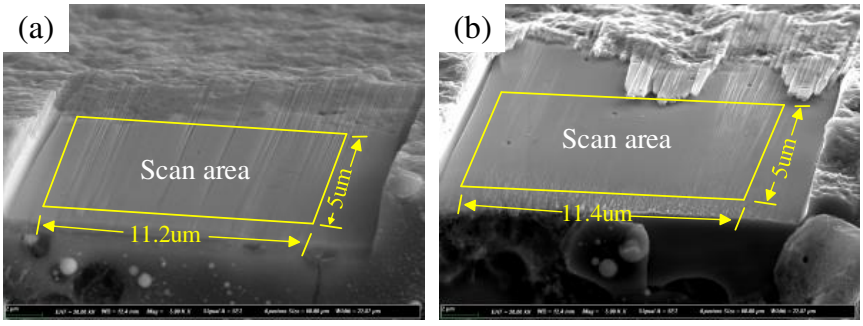

Fig.8. The FIB processed observation sites: (a) observation site 1 (b) observation site 2

The longitudinal section on which the third observation site was located was carefully polished by using 600#, 800#, 1000#, 1200#, 1500#, 2000#, 3000#, and 5000# sandpaper for preliminary grinding, followed by 5, 3.5, and 0.5 μm diamond polishing paste to remove the surface small scratches. Lastly, 0.05 and 0.02 micron silica fine polishing liquid was used for final finish.

After the surface processing, the samples were observed under the Gemini SEM-500 ultra-high resolution scanning electron microscope produced by German Carl Zeiss, the adopted camera was the EBSD camera produced by Oxford Instruments.

4. Results and discussion

4.1 KAM and GROD

The KAM distributions at the first and the second observation sites are separately shown in Fig.9(a) and Fig 9(b). It can be seen that the KAM degree fraction at both sites conformed to normal distribution. The highest degree fraction at the first site corresponded to about 0.3 degree, and that

of the second site corresponded to 0.4 degree. The second observation site, which was closer to the initiation pore, had a relatively higher KAM value. Since KAM is closely related to local deformation, it can be seen that the local lattice deformation at the fish-eye region is enhanced when getting closer to the initiation site.

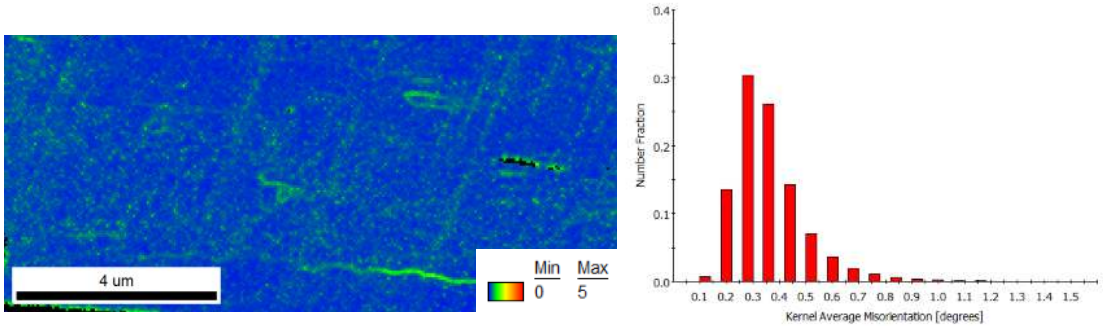

(a)

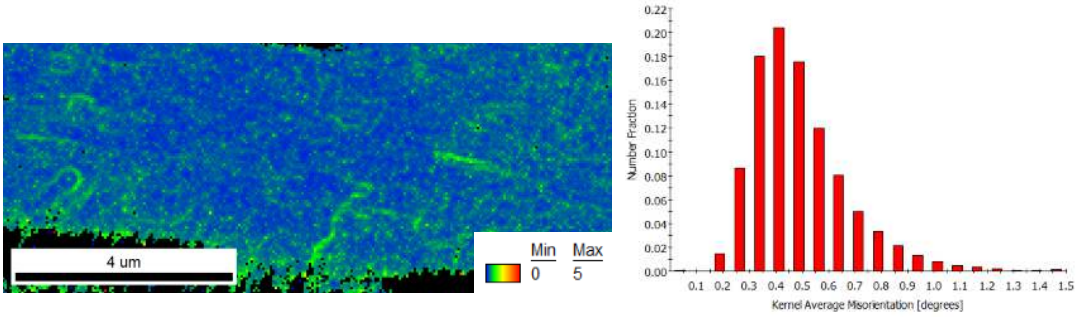

(b)

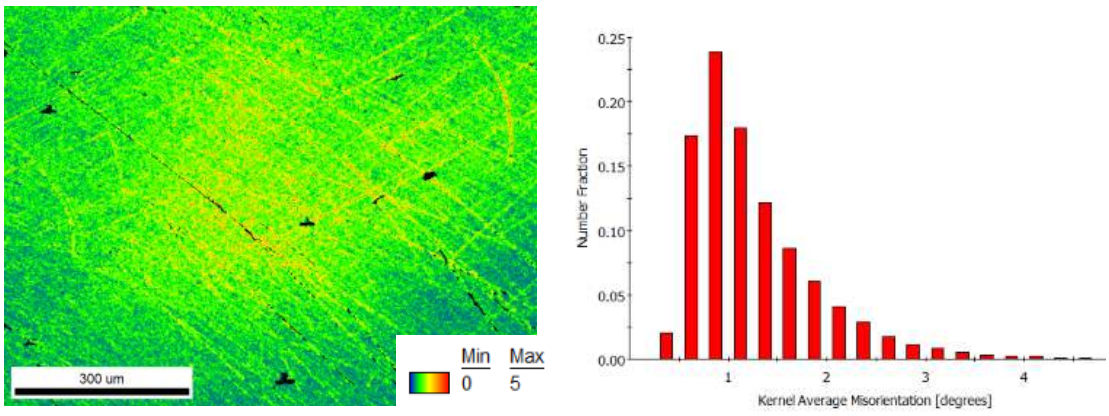

(c)

Fig.9. The KAM distribution of (a) observation site 1, (b) observation site 2 and (c) observation

site 3.

The KAM distribution at the third observation site, which was right below the initiation pore, is shown in Fig.9 (c). It can be seen clearly that the highest degree fraction at this site corresponded to near 1 degree, which is higher than the first and the second sites. It suggests that the local deformation in the vertical direction was stronger than that in the parallel section.

The GROD distribution of the first and the second sites is shown in Fig.10. In both sites, the maximum GROD value was located near the central line (the cutting side) of the initiation pore. The GROD distribution of both sites did not show obvious difference. Since the GROD is a parameter used to show the local orientation inhomogeneity by quantifying the reference misorientation degree (in this paper, the lowest KAM value is taken as the reference point), it can be concluded that the relative misorientation in the fish-eye region was comparatively homogeneous, which was different from the local deformation represented by KAM.

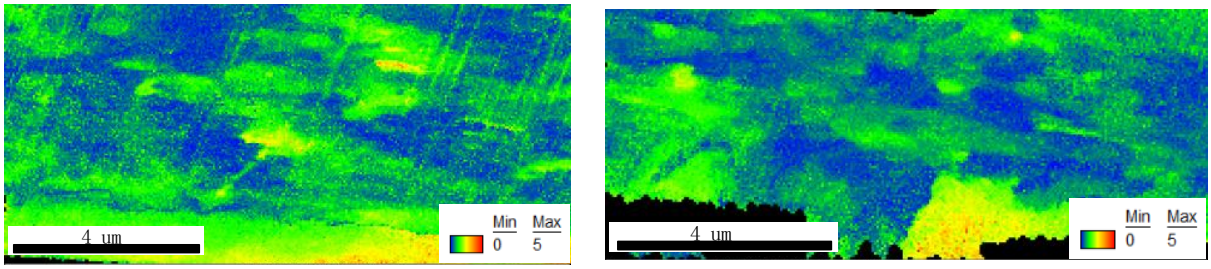

(a) (b)

Fig.10. The GROD of (a) the first observation site and (b) the second observation site

The GROD distribution of the third observation site is shown in Fig.11. It can be seen from the diagram that the GROD value had a distinct inhomogeneous distribution. The scanning area was much bigger than the FIB processed area, and this explains why the misorientation gradient was more obvious in this region. The GROD value reached the highest near the origin site, and gradually decreased in the direction deviating from the origin side. To have a more intuitive description of the

changing of GROD, a deviating path is marked in the diagram, and three distinct points on the path are highlighted to show the local lattice orientation. The relative orientation change in respect to the origin point as well as the point-to-point orientation change on the deviating path are shown in Fig.11(b). The point-to-point orientation change fluctuates near the one-degree level line, but maintains comparatively stable. The point-to-origin orientation change keeps growing on this path, indicating that the intense plastic behavior at the initiation site leads to severe “long-range” lattice deformation. By combing with the KAM distribution shown in Fig.9, it can be concluded that total deformation at the initiation site can be the sum of two parts: the local deformation which is related to the local lattice motion, and the reference deformation with respect to the original crystal coordinate system, as shown in Fig.12. It indicates that the plastic motion at the initiation site is complex, and the lattice deforms not only locally but also globally.

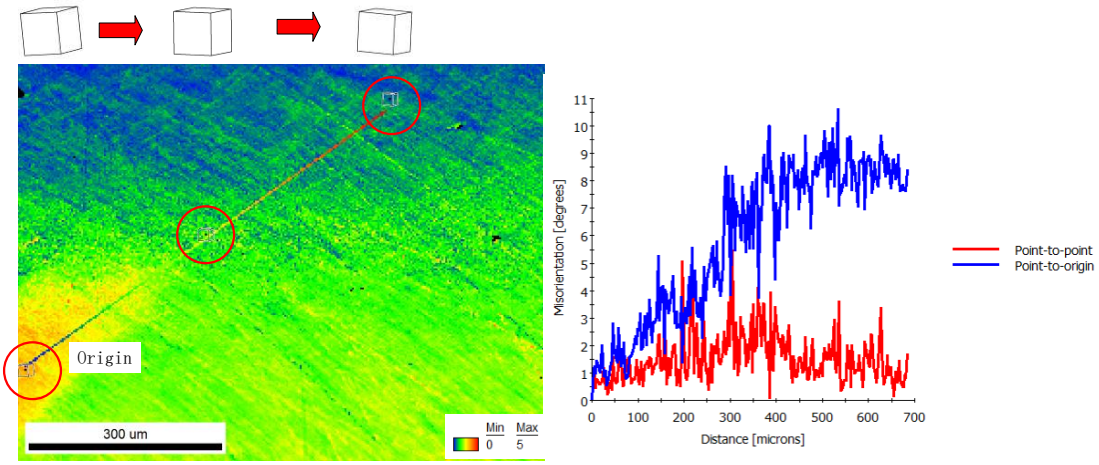

(a) (b)

Fig.11. The GROD of the third observation site

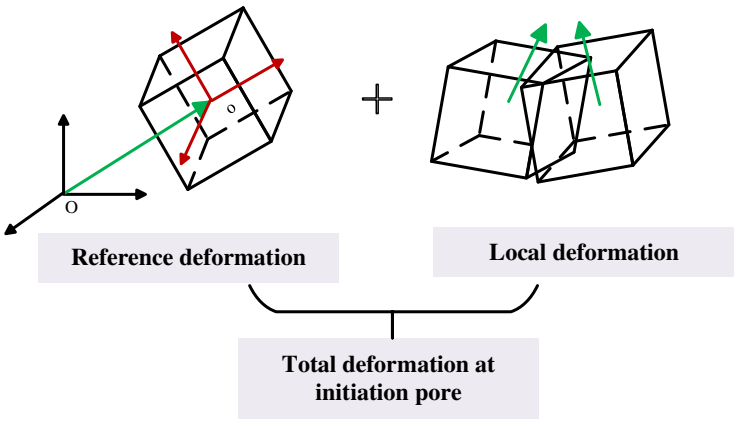

Fig.12. The schematic of the total deformation at the initiation pore

4.2 GND

In order to analyze the GND density distribution, the original orientation data taken from the observation site 1 (Fig.7) are post-processed according to the method introduced in Section 3.2. Firstly, the orientation data of every scanning point can be obtained through the EBSD observation, then the dislocation theory presented in Section 3.2 is introduced into a self-developed Matlab program. The GND dislocation of different dislocation types can be calculated for every point, and the final GND dislocation map is obtained by using a self-defined dislocation parameter output in this program.

It should be mentioned that the crystal coordinate system is supposed to be defined in this analysis. Since the original test bars were casted with an axial crystal orientation of [001], the orientation which is perpendicular to the fracture plane is defined as the natural crystal [001] orientation. The distinct dendrite arm (Fig.4 (b)) shown on the fracture plane is used as a reference to define the [100]-[010] orientation. Since the nickel-base single crystal has a face-centered cubic structure, and the [100] orientation is totally symmetric to the [010] orientation, therefore, these two orientations can be interchangeable. Without loss of generality, the dendrite arm direction which is

parallel with the cutting direction is defined as the [010] orientation, and another direction which is perpendicular to the cutting direction is defined as the [100] orientation, as shown in Fig.14(a).

Fig.13 shows the calculated dislocation density distribution on different slip systems. The slip plane $(\bar{1}11)$ with two slip directions $[01\bar{1}]$ and $[\bar{1}\,\bar{1}0]$ have shown to be the slip plane with the maximum edge dislocation density, and the screw dislocation peaks at the $[\bar{1}\,\bar{1}0]$ direction.

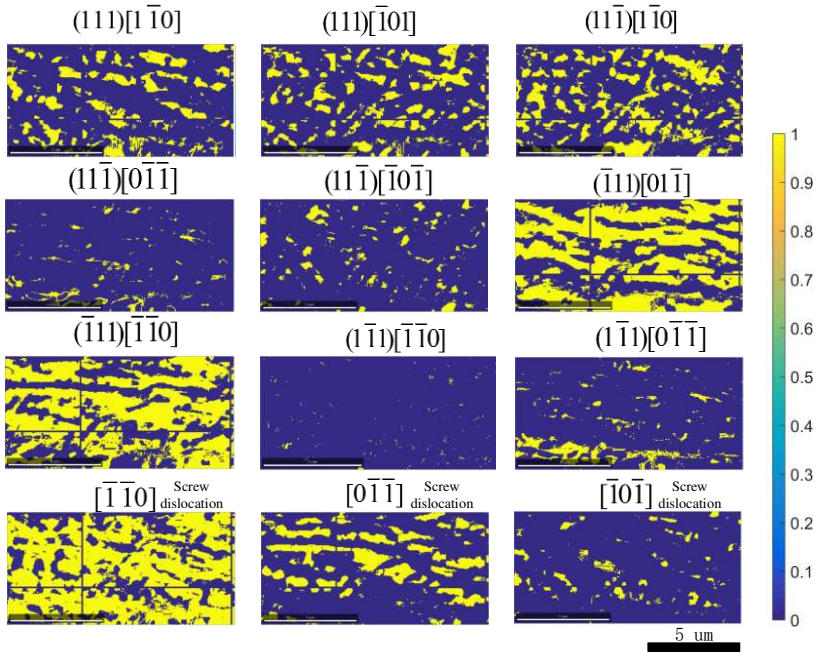

Fig.13. The dislocation density on different slip systems

GND refers to the dislocations appeared in strain gradient fields due to geometrical constraints of the crystal lattice in crystals. NBSX is constructed by one single crystal and its lattice structure is continuous. The curvature degree of lattice at different parts can be effectively reflected by the magnitude of GND density. In a sense, the GND density is positively correlated with the plastic deformation and therefore can be used as a reflection of internal plastic deformation.

NBSX is typical face-centered cubic(FCC) crystal, and the slip along natural slip systems of FCC structure has been widely reported as a dominant failure mode in the fatigue deformation of NBSX [7,17,69]. Therefore, it is significant to analyze the GND density on each slip system, which

can be an effective way to track the dislocation motion as well as to estimate the deformation degree in the fatigue process.

According to the calculated results shown in Fig.13, the GND density on the slip plane $(\bar{1}11)$ is obviously higher than that on other planes, which suggests that the lattice deformation accumulation based on this plane is faster and easier, and the dislocation motion is more intense. In the fatigue failure process of NBSX, multiple slip systems are potential to be activated and generally there exists a dominant slip system which encounters the severest damage and determines the crack initiation direction. The relation between the GND density and the slip motion is further analyzed in Section 4.3.

4.3 Discussion

(1) The analysis of KAM/GROD results

The KAM and GROD are crystal orientation characterization parameters which can be useful to reestablish the fatigue failure process. For single crystal materials, the fatigue process is accompanied by intense lattice deformation, which is a result of internal dislocation accumulation. The lattice deformation degree can be reflected by the magnitude of orientation change, and a larger orientation change suggests a severer deformation state.

As introduced in Section 3.1, KAM is used to characterize the local orientation gradient, and it is a reflection of the local deformation degree. GROD is defined as the orientation deviation between a target point and a reference point, and it is used to characterize the intracrystalline inhomogeneity degree of orientation. By combining the different characterization function of these two parameters, the deformation status represented by lattice curvature can be well presented.

In the fish-eye region of the tested NBSX, the observation site which is closer to the initiation pore shows a higher KAM value, it can be seen that the local lattice deformation at the fish-eye region is enhanced when getting closer to the initiation site. Different from the KAM, the local orientation inhomogeneity represented by the value of GROD does not show obvious dependence on the distance from the initiation pore in the fish-eye region. However, when observed from a larger scale, the GROD shows an obvious gradient from the initiation pore to far-field region, which indicates that the fish-eye deformation center encounters severe lattice distortion with respect to the far-field lattice structure in the damage process. By combining the results of KAM and GROD, it can be concluded that total deformation at the fish-eye center can be separated into the local deformation and the reference deformation, and the reference deformation is severer.

(2) The relation between the crack initiation direction and the dislocation density

In order to analyze the relation between the crack initiation direction and the dislocation density, the fracture feature is further analyzed in Fig.14(a). Under the scanning electron microscope, the main crack initiation direction could be clearly identified, which is about 45 degrees inclined to the [100] direction in the crystal coordinate system, as shown in Fig.14(a).

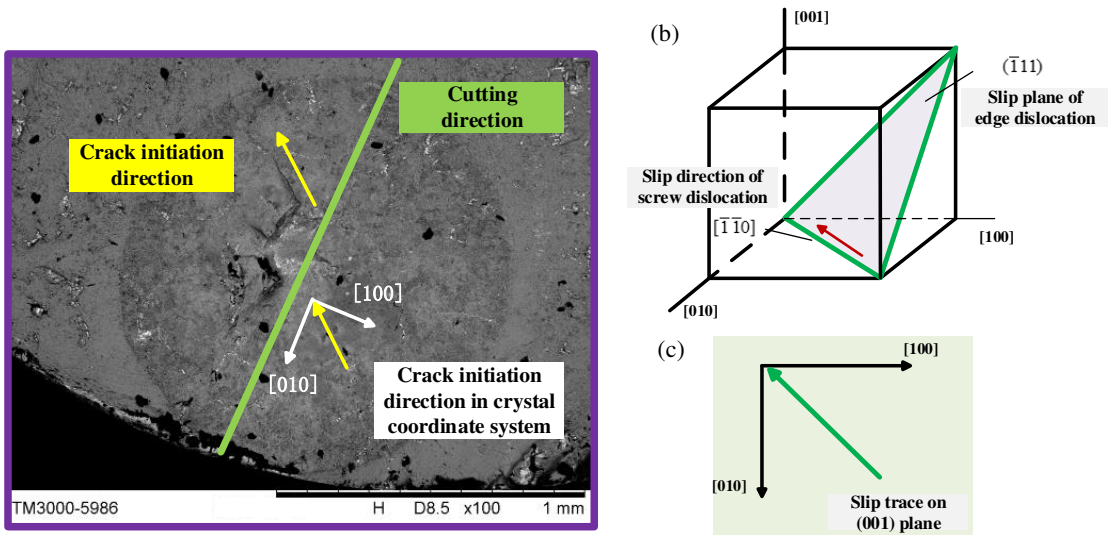

(a)

Fig.14. The crack initiation direction analysis

The slip trace of the slip plane $(\bar{1}11)$ on which the dislocation density peaks is analyzed in Fig.14(b) and Fig.14(c). It can be seen that on the (001) plane, which is exactly the fracture plane, the slip trace caused by the motion of the slip plane $(\bar{1}11)$ is a line with 45 degrees inclined to the [100] direction. This is in agreement with the crack initiation direction in Fig.14(a). The slip direction of the screw dislocation is in the $[\bar{1}\,\bar{1}0]$ direction, which is also in agreement with the crack initiation direction. Therefore, it can be concluded that the slip direction on which the dislocation density reaches the maximum determines the crack initiation direction of NBSX under the investigated background.

5. Conclusions

In this paper, the fatigue limit of nickel-base single crystal is experimentally studied. The fatigue failure is revealed as pore-induced crack initiation, and the observed fish-eye region around the initiation pore is studied by adopting the EBSD method. The main conclusions can be drawn as follows:

(1) Under the test condition of an elevated temperature of 980°C, the fatigue limit of the second generation nickel-base single crystal DD5 with the specific heat treatment and casting method is revealed as 432.5MPa.

(2) The fracture analysis results show that casting pores are the crack initiation sites under the investigated background. Distinct fish-eye feature is observed around the crack initiation pore. By conducting microscopic exploration in the fish-eye region under the adoption of EBSD, it is revealed that severe plastic behavior occurs around the initiation pore accompanied by crystalline orientation deviation. The total deformation around the pore can be dissolved into local deformation represented

by local misorientation motion and reference deformation represented by global misorientation motion.

(3) The natural slip systems of face-centered cubic crystals are the slip deformation foundation of the nickel-base single crystal material. The slip trace caused by the motion of slip plane can be used as a reference to determine the dominant slip direction. The analysis result of geometrically necessary dislocation density on different slip system shows that the slip direction in which the dislocation density reaches the maximum agrees with the observed fatigue crack initiation direction.

Declaration of Competing Interest

The authors declare that they have no known competing financial interests or personal relationships that could have appeared to influence the work reported in this paper.

Acknowledgment

The National Science and Technology Major Project (Grant No.2017-VI-0003-0073) and the National Natural Science Foundation of China (Grant No. 12002155) are acknowledged for supporting the present research work.

References

[1] Reed RC. The Superalloys: Fundamentals and Applications. Cambridge University Press; 2006.

[2] Al-Jarba KA, Fuchs GE. Elevated temperature, high cycle fatigue behavior of carbon-containing single crystal Ni-Based superalloys. Mater Sci Eng A 2019;760:287-95. https://doi.org/10.1016/j.msea.2019.05.113

[3] Jiang W, Li P, Yao WX, Rui SS, Shi HJ, Huang J. The effect of porosity size on the high cycle fatigue life of nickel-based single crystal superalloy at 980°C. Int J Fatigue 2021;147:106191. https://doi.org/10.1016/j.ijfatigue.2021.106191

[4] Arakere NK. High Temperature Fatigue Properties of Single Crystal Superalloys in Air and Hydrogen. J Eng Gas Turb Power 2004;126(3):590-603.

[5] Sun J, Yang S, and Yuan H. Assessment of thermo-mechanical fatigue in a nickel-based single-crystal superalloy CMSX-4 accounting for temperature gradient effects. Mater Sci Eng A

2021;809:140918. https://doi.org/10.1016/j.msea.2021.140918

[6] Li P, Jiang W, Rui S-S, Yao W-x, Shi H-j, Han Q-n, et al. Effect of misorientation on the fatigue life of nickel-base single crystal superalloy DD5 at 980 °C. Int J Fatigue 2021;153:106479. https://doi.org/10.1016/j.ijfatigue.2021.106479

[7] Li P, Yao W, and Jiang W. Orientation-dependent low cycle fatigue performance of Nickel-base single crystal superalloy at intermediate temperature range. Mater Today Commun 2021;26:101836. https://doi.org/10.1016/j.mtcomm.2020.101836

[8] Li P, Yao W, Shi H, Luo P, and Hua Y. A topologized resolved shear stress method for the life prediction of nickel-base single crystal superalloys. Theor Appl Fract Mech 2020;108:102624. https://doi.org/10.1016/j.tafmec.2020.102624

[9] Antolovich BF, Saxena A, and Antolovich SD. Fatigue crack propagation in single-crystal CMSX- 2 at elevated temperature. J Mater Eng Perform 1993;2(4):489-95. https://doi.org/10.1007/BF02661731

[10] Busse C, Gustafsson D, Palmert F, Sjödin B, Almroth P, Moverare JJ, et al. Criteria evaluation for the transition of cracking modes in a single-crystal nickel-base superalloy. Theor Appl Fract Mech 2020;106:102453. https://doi.org/10.1016/j.tafmec.2019.102453

[11] Chen X, and Sakaguchi M. Transition behavior from Mode I cracking to crystallographic cracking in a Ni-base single crystal superalloy. Int J Fatigue 2020;132:105400. https://doi.org/10.1016/j.ijfatigue.2019.105400

[12] Suzuki S, Sakaguchi M, and Inoue H. Temperature dependent fatigue crack propagation in a single crystal Ni-base superalloy affected by primary and secondary orientations. Mater Sci Eng A 2018;724:559-65. https://doi.org/10.1016/j.msea.2018.03.090

[13] Neu RW. Crack paths in single-crystal Ni-base superalloys under isothermal and thermomechanical fatigue. Int J Fatigue 2019;123:268-78. https://doi.org/10.1016/j.ijfatigue.2019.02.022

[14] Moverare JJ, Johansson S, and Reed RC. Deformation and damage mechanisms during thermal–mechanical fatigue of a single-crystal superalloy. Acta Mater 2009;57(7):2266-76. https://doi.org/10.1016/j.actamat.2009.01.027

[15] Pierce CJ, Palazotto AN, and Rosenberger AH. Creep and fatigue interaction in the PWA1484 single crystal nickel-base alloy. Mater Sci Eng A 2010;527(29):7484-9. https://doi.org/10.1016/j.msea.2010.08.033

[16] Lamm M, and Singer RF. The Effect of Casting Conditions on the High-Cycle Fatigue Properties of the Single-Crystal Nickel-Base Superalloy PWA 1483. Metall Mater Trans A 2007;38(6):1177-83. https://doi.org/10.1007/s11661-007-9188-4

[17] Levkovitch V, Sievert R, and Svendsen B. Simulation of deformation and lifetime behavior of a fcc single crystal superalloy at high temperature under low-cycle fatigue loading. Int J Fatigue 2006;28(12):1791-802. https://doi.org/10.1016/j.ijfatigue.2005.12.006

[18] Ding ZP, Li M, and Wang TF. Analysis of Multiaxial Low Cycle Fatigue Life for Single Crystal Ni-Based Superalloy Based on Two-Phase Unit Cell Model. Appl Mech Mater 2012;117-119:503-8.

[19] Ranjan S, and Arakere NK. A Fracture-Mechanics-Based Methodology for Fatigue Life Prediction of Single Crystal Nickel-Based Superalloys. J Eng Gas Turb Power 2008;130(3):32501.

[20] Sakaguchi M, and Okazaki M. Fatigue life evaluation of a single crystal Ni-base superalloy,

accompanying with change of microstructural morphology. Int J Fatigue 2007;29(9):1959-65.
[21] Wan JS, and Yue ZF. A low-cycle fatigue life model of nickel-based single crystal superalloys under multiaxial stress state. Mater Sci Eng A 2005;392(1):145-149. https://doi.org/10.1016/j.msea.2004.09.069
[22] Li SX and D. J. Smith. High temperature fatigue-creep behaviour of single crystal SRR99 nickel base superalloys: Part II-fatigue-creep life behavior. Fatigue Fract Eng M 1995; 18(5) : 631-643. https://doi.org/10.1111/j.1460-2695.1995.tb01423.x
[23] Brien V, and Décamps B. Low cycle fatigue of a nickel based superalloy at high temperature: deformation microstructures. Mater Sci Eng A 2001; 316(1):18-31. https://doi.org/10.1016/S0921-5093(01)01235-7
[24] Morrissey RJ, and Golden PJ. Fatigue strength of a single crystal in the gigacycle regime. Int J Fatigue 2007;29(9):2079-84. https://doi.org/10.1016/j.ijfatigue.2007.04.003
[25] Leverant GR, and Gell M. The influence of temperature and cyclic frequency on the fatigue fracture of cube oriented nickel-base superalloy single crystals. Metall Trans A 1975;6(2):367. https://doi.org/10.1007/BF02667291
[26] Zhang Y, Shi H, Gu J, Li C, Kadau K, and Luesebrink O. Crystallographic analysis for fatigue small crack growth behaviors of a nickel-based single crystal by in situ SEM observation. Theor Appl Fract Mech 2014;69:80-9. https://doi.org/10.1016/j.tafmec.2013.11.002
[27] Belyaev MS, and Petrushin NV. High-Cycle Fatigue of Single Crystals of Nickel-Base Superalloy VZhM4. Inorg Mater 2018;9(4):655-62. https://doi.org/10.1134/S2075113318040044
[28] Belyaev MS, Morozova LV, Gorbovets MA, and Slavin AV. High-Cycle Fatigue of Single-Crystal Heat-Resistant Nickel Alloy under the Conditions of Stress Concentration. Metallurgist 2020;63(11):1237-47. https://doi.org/10.1007/s11015-020-00946-5
[29] Jiang W, Li P, Yao W-X, Rui S-S, Shi H-J, and Huang J. The effect of porosity size and oxidation on the HCF property of nickel-based single crystal superalloy at 980 °C. Theor Appl Fract Mech 2022;120:103423. https://doi.org/10.1016/j.tafmec.2022.103423
[30] Cervellon A, Hémery S, Kürnsteiner P, Gault B, Kontis P, and Cormier J. Crack initiation mechanisms during very high cycle fatigue of Ni-based single crystal superalloys at high temperature. Acta Mater 2020;188:131-44. https://elkssl0a75e822c6f3334851117f8769a30e1cportal.i.nuaa.edu.cn:4443/10.1016/j.actamat.2020.02.012
[31] Hong Y, Lei Z, Sun C, and Zhao A. Propensities of crack interior initiation and early growth for very-high-cycle fatigue of high strength steels. Int J Fatigue 2014;58:144-51. https://doi.org/10.1016/j.ijfatigue.2013.02.023
[32] Li YD, Zhang LL, Fei YH, Liu XY, and Li MX. On the formation mechanisms of fine granular area (FGA) on the fracture surface for high strength steels in the VHCF regime. Int J Fatigue 2016;82:402-10. https://doi.org/10.1016/j.ijfatigue.2015.08.021
[33] Grad P, Reuscher B, Brodyanski A, Kopnarski M, and Kerscher E. Mechanism of fatigue crack initiation and propagation in the very high cycle fatigue regime of high-strength steels. Scripta Mater 2012;67(10):838-41. https://doi.org/10.1016/j.scriptamat.2012.07.049
[34] Heinz S, and Eifler D. Crack initiation mechanisms of Ti6Al4V in the very high cycle fatigue regime. Int J Fatigue 2016;93:301-8. https://doi.org/10.1016/j.ijfatigue.2016.04.026
[35] Sakai T. Review and Prospects for Current Studies on Very High Cycle Fatigue of Metallic

Materials for Machine Structural Use. J Solid Mech Mater Eng 2009;3(3):425-39. https://doi.org/10.1299/jmmp.3.425

[36] Shiozawa K, Morii Y, Nishino S, and Lu L. Subsurface crack initiation and propagation mechanism in high-strength steel in a very high cycle fatigue regime. Int J Fatigue 2006;28(11):1521-32. https://doi.org/10.1016/j.ijfatigue.2005.08.015

[37] Murakami Y, Nomoto T, and Ueda T. Factors influencing the mechanism of superlong fatigue failure in steels. Fatigue Fract Eng M 1999;22(7):581–90.

[38] Shanyavskiy AA. Mechanisms and modeling of subsurface fatigue cracking in metals. Eng Fract Mech 2013;110:350-63. https://doi.org/10.1016/j.engfracmech.2013.05.013

[39] Hong Y, Liu X, Lei Z, and Sun C. The formation mechanism of characteristic region at crack initiation for very-high-cycle fatigue of high-strength steels. Int J Fatigue 2016;89:108-18. https://doi.org/10.1016/j.ijfatigue.2015.11.029

[40] Liu YB, Li SX, Li YD, and Yang ZG. Factors influencing the GBF size of high strength steels in the very high cycle fatigue regime. Mater Sci Eng A 2011;528(3):935-42. https://doi.org/10.1016/j.msea.2010.10.017

[41] Li YD, Chen SM, Liu YB, Yang ZG, Li SX, Hui WJ, et al. The characteristics of granular-bright facet in hydrogen pre-charged and uncharged high strength steels in the very high cycle fatigue regime. J Mater Sci 2010;45(3):831-41. https://doi.org/10.1007/s10853-009-4007-5

[42] Shiozawa K, Hasegawa T, Kashiwagi Y, and Lu L. Very high cycle fatigue properties of bearing steel under axial loading condition. Int J Fatigue 2009;31(5):880-8. https://doi.org/10.1016/j.ijfatigue.2008.11.001

[43] Rui SS, Shang YB, Su Y, Qiu W, Niu L-S, Shi HJ, et al. EBSD analysis of cyclic load effect on final misorientation distribution of post-mortem low alloy steel: A new method for fatigue crack tip driving force prediction. Int J Fatigue 2018;113:264-76. https://doi.org/10.1016/j.ijfatigue.2018.04.016

[44] Sarkar A, Dash MK, Nagesha A, Dasgupta A, Sandhya R, and Okazaki M. EBSD based studies on various modes of cyclic deformation at 923 K in a type 316LN stainless steel. Mater Sci Eng A 2018;723:229-37. https://doi.org/10.1016/j.msea.2018.02.101

[45] Carneiro Í, and Simões S. Recent Advances in EBSD Characterization of Metals. Metals 2020;10(8). https://doi.org/10.3390/met10081097

[46] Rui SS, Shang YB, Qiu W, Niu LS, Shi HJ, Matsumoto S, et al. Fracture mode identification of low alloy steels and cast irons by electron back-scattered diffraction misorientation analysis. J Mater Sci Tech 2017;33(12):1582-95. https://doi.org/10.1016/j.jmst.2017.03.020

[47] Chen P, Mao SC, Liu Y, Wang F, Zhang YF, Zhang Z, et al. In-situ EBSD study of the active slip systems and lattice rotation behavior of surface grains in aluminum alloy during tensile deformation. Mater Sci Eng A 2013;580:114-24. https://doi.org/10.1016/j.msea.2013.05.046

[48] Li S, Guo C, Hao L, Kang Y, and An Y. In-situ EBSD study of deformation behaviour of 600 MPa grade dual phase steel during uniaxial tensile tests. Mater Sci Eng A 2019;759:624-32. https://doi.org/10.1016/j.msea.2019.05.083

[49] Zhang W, Lu J, Wang J, Sang L, Ma J, Zhang Y, et al. In-situ EBSD study of deformation behavior of Inconel 740H alloy at high-temperature tensile loading. J Alloys Compd 2020;820:153424. https://doi.org/10.1016/j.jallcom.2019.153424

[50] Jiang W, Junxia L, Li F, Wang J, Zhang Y, Zhang Z, et al. In-situ EBSD investigation of the effect of orientation on plastic deformation behavior of a single crystal superalloy. Mater Sci

Eng A 2022:143453. https://doi.org/10.1016/j.msea.2022.143453
[51] Rui SS, Shang YB, Fan YN, Han QN, Niu LS, Shi HJ, et al. EBSD analysis of creep deformation induced grain lattice distortion: A new method for creep damage evaluation of austenitic stainless steels. Mater Sci Eng A 2018;733:329-37. https://doi.org/10.1016/j.msea.2018.07.058
[52] Kobayashi D, Miyabe M, Kagiya Y, Sugiura R, and Yokobori AT. An Assessment and Estimation of the Damage Progression Behavior of IN738LC under Various Applied Stress Conditions Based on EBSD Analysis. Metall Mater Trans A 2013;44(7):3123-35. https://doi.org/10.1007/s11661-013-1677-z
[53] Kobayashi D, Miyabe M, and Achiwa M. ASME Turbo Expo 2015: Turbine Technical Conference and Exposition. 2015.
[54] Baek M-S, Kim K-S, Park T-W, Ham J, and Lee K-A. Quantitative phase analysis of martensite-bainite steel using EBSD and its microstructure, tensile and high-cycle fatigue behaviors. Mater Sci Eng A 2020;785:139375. https://doi.org/10.1016/j.msea.2020.139375
[55] Uematsu Y, Kakiuchi T, Tamada K, and Kamiya Y. EBSD analysis of fatigue crack initiation behavior in coarse-grained AZ31 magnesium alloy. Int J Fatigue 2016;84:1-8. https://doi.org/10.1016/j.ijfatigue.2015.11.010
[56] Ruttert B, Meid C, Mujica Roncery L, Lopez-Galilea I, Bartsch M, and Theisen W. Effect of porosity and eutectics on the high-temperature low-cycle fatigue performance of a nickel-base single-crystal superalloy. Scr Mater 2018;155:139-43. https://doi.org/10.1016/j.scriptamat.2018.06.036
[57] Han QN, Rui SS, Qiu W, Ma X, Su Y, Cui H, et al. Crystal orientation effect on fretting fatigue induced geometrically necessary dislocation distribution in Ni-based single-crystal superalloys. Acta Mater 2019;179:129-41. https://doi.org/10.1016/j.actamat.2019.08.035
[58] Miller, and O'donnell. The fatigue limit and its elimination. Fatigue Fract Eng M 1999;22(7):545-57. https://doi.org/10.1046/j.1460-2695.1999.00204.x
[59] Sadeghi F, Kermanpur A, and Norouzi E. Optimizing Grain Selection Design in the Single-Crystal Solidification of Ni-Based Superalloys. Cryst Res Technol 2018;53(12):1800108. https://doi.org/10.1002/crat.201800108
[60] Hu S, Liu L, Yang W, Sun D, Huo M, Huang T, et al. Formation of Accumulated Misorientation During Directional Solidification of Ni-Based Single-Crystal Superalloys. Metall Mater Trans A 2019;50(4):1607-10. https://doi.org/10.1007/s11661-018-05109-5
[61] Dong C, Yu H, Li Y, Yang X, and Shi D. Life modeling of anisotropic fatigue behavior for a single crystal nickel-base superalloy. Int J Fatigue 2014;61:21-7. https://doi.org/10.1016/j.ijfatigue.2013.11.026
[62] Li SX, Ellison EG, and Smith DJ. The influence of orientation on the elastic and low cycle fatigue properties of several single crystal nickel base superalloys. J Strain Anal Eng 1994;29(2):147-53. https://doi.org/10.1243/03093247V292147
[63] Yao WX. Fatigue life estimation of structures. Beijing: Science Press; 2019.
[64] Murakami Y, and Beretta S. Small Defects and Inhomogeneities in Fatigue Strength: Experiments, Models and Statistical Implications. Extremes 1999;2(2):123-47. https://doi.org/10.1023/A:1009976418553
[65] Nicoletto G, Konečná R, and Fintova S. Characterization of microshrinkage casting defects of Al-Si alloys by X-ray computed tomography and metallography. Int J Fatigue 2012;41:39-46.

[66] Cho JH, Rollett AD, and Oh KH. Determination of a mean orientation in electron backscatter diffraction measurements. Metall Mater Trans A 2005;36(12):3427-38. https://doi.org/10.1007/s11661-005-0016-4

[67] Nye JF. Some geometrical relations in dislocated crystals. Acta Metall 1953;1(2):153-62. https://doi.org/10.1016/0001-6160(53)90054-6

[68] Ashby MF. The deformation of plastically non-homogeneous materials. The Philos Mag A 1970;21(170):399-424. https://doi.org/10.1080/14786437008238426

[69] Shi D, Huang J, Yang X, and Yu H. Effects of crystallographic orientations and dwell types on low cycle fatigue and life modeling of a SC superalloy. Int J Fatigue 2013; 49:31-39. https://doi.org/10.1016/j.ijfatigue.2012.12.005